

Investigation of cross-field wavefront aberrations of KrF lithography exposure systems as a function of excimer laser bandwidth^[1]

Ivan Lalovic, Armen Kroyan, Nigel Farrar, Dennis Taitano[†], Paolo Zambon, Adlai Smith[‡]

Cymer, Inc., 16750 Via Del Campo Ct., San Diego, CA 92127

[†]KLA-Tencor, 160 Rio Robles, San Jose, CA 95134

[‡]Litel Instruments, 6142 Nancy Ridge Drive, San Diego, CA 92121

ABSTRACT

Quantification of projection lens aberrations in lithographic exposure systems has gained significant importance due to more stringent critical dimension control and image fidelity requirements. As linewidths shrink, the impacts of wavefront aberrations on imaging become more pronounced. Therefore, minimization of the wavefront aberrations across the image field is desired and has led to the development of a number of measurement approaches. The proposed techniques have been evaluated extensively for characterization and specification of lens systems, adjustments, matching, and periodic control and monitoring of lithography systems for volume production.

In this study, we discuss the contribution of excimer laser bandwidth towards lens aberrations. We carry out simulations of the effects of image contrast on conventional projection patterning, to evaluate the degree of aberration-induced linewidth changes depending on image contrast level. Also, experiments have been conducted to measure the response of wavefront error as a function of spectral bandwidth for a 0.6NA stepper and scanner. Depending on the field location, a positive relationship is observed between the measured aberration level and bandwidth. We propose a formalism to correlate the aberration measurement with aberration response to wavelength offset, presented elsewhere.[2] The wavefront error, in this work, is measured using a commercially available in-situ interferometric technique, whose response is largely insensitive to focal plane changes and partial coherence.

Keywords: lithography, aberration, Zernike, excimer laser, spectral bandwidth

1. INTRODUCTION

The problem of critical dimension (CD) control in lithographic patterning of photoresist is growing in importance as linewidths decrease. Due to the diminishing physical tolerances of the CMOS IC device, the scaling of critical dimension control, across the image field, for performance-driven applications is becoming more rapid than the scaling of nominal linewidths. Accordingly, photolithography manufacturing of performance-driven IC devices must continue to increase the scale of effort directed toward control of critical dimensions across the semiconductor device circuit.

As linewidths are reduced, the setup of the exposure system, and especially the projection lens, can contribute measurable effects to cross-field CD control and image fidelity.[3-5] Although, the projection lens aberrations can be measured accurately using Phase Measuring Interferometry (PMI),[6,7] this technique is typically applied during lens manufacturing and set-up in the factory. PMI has not found wide application for in-situ aberration measurement and set-up of the lens within the exposure system (stepper or scanner) installed in the field. Lithographers have therefore resorted to measuring photoresist image response in order to infer the level of lens aberrations. These techniques have typically employed clever feature (object) designs on the reticle that, when imaged in photoresist, exhibit enhanced sensitivity.[8-11] Such approaches evaluate the aberration impact on the aerial image, under the specific imaging conditions, sampled in the photoresist response. The measurement is

typically carried out by SEM image-processing of the photoresist feature. However, other imaging factors such as field curvature, partial coherence, vibrations, flare, substrate reflectivity/topography, also strongly influence the projected aerial image and therefore lead to measurement error. In this work, we vary the bandwidth of the KrF excimer laser beam in order to understand the contribution of the laser spectrum to the measured aberration using a commercially available aberration-measurement method, based on the Shack-Hartman interferometer.[12-14] The image contrast of the diagnostic feature in this technique is largely insensitive to defocus, coherence and other factors listed above, and is therefore suitable for measurement of the effects of excimer laser bandwidth on aberration levels. In this paper we use the arrangement of Zernike polynomials according to ref. 15.

2. LITHOGRAPHY MODELING AND THEORY PREDICTIONS

2.1 Chromatic aberration and lens response

Due to optical materials constraints, dioptric DUV (KrF and ArF) lens designs of modern exposure systems, made of primarily fused silica (SiO_2) and CaF, to a large degree, cannot be compensated for material dispersion. The lack of chromatic correction requires the application of highly line-narrowed excimer lasers with sub-picometer spectral widths. Figure 1, below, shows the behavior of the focus (Z_4) Zernike coefficient as a function of illumination wavelength for a 0.6NA Nikon S-202 DUV lithography scanner, measured using the Litel in-situ (*inspec-step*) interferometer.[12] In this work, the diagnostic photoresist image is formed by projecting a large encoded pattern (several microns in size) through an aperture placed between the reticle and the objective lens. Therefore, each feature in the diagnostic image is formed by an aperture-limited portion of the pupil and corresponds to a particular ray angle. The displacement of these features is proportional to the average wavefront gradient in that region of the pupil and is measured, using an in-line optical overlay system, relative to normally imaged reference patterns.[12-14] The response of the 28 Zernike coefficients to center wavelength offset, for several lens designs, has been measured and is reported elsewhere.[2,14]

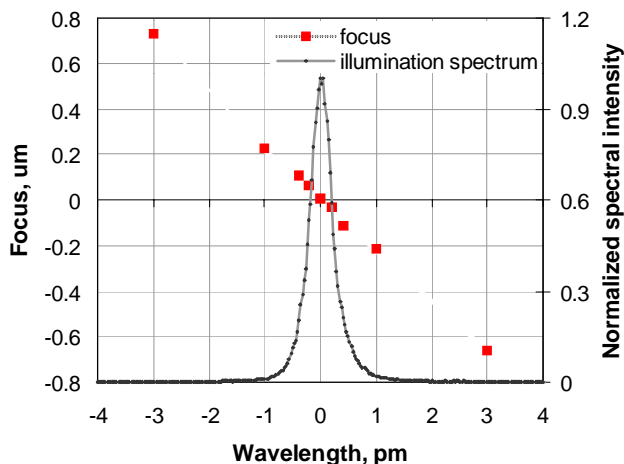


Figure 1. Focus, illumination spectral shape

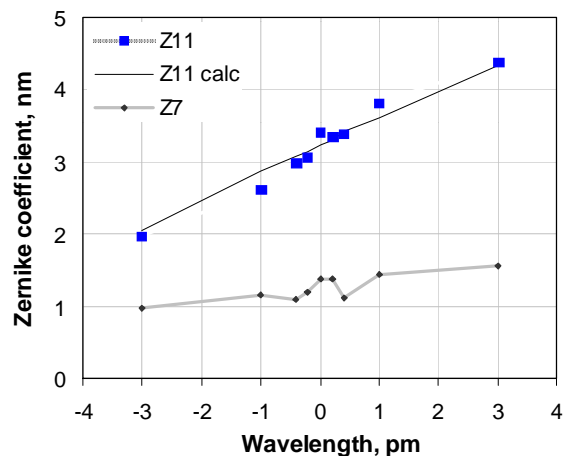


Figure 2. 3rd-order spherical, primary coma

In figure 1, on the right-hand y-axis, we also plot the illumination spectrum of a KrF laser source. Therefore, we see that even the highly line-narrowed excimer lasers contribute to an effective defocusing of the image. The empirical relationship between defocus and wavelength above, termed longitudinal chromatic aberration, can be related by a linear fit, yielding a slope of $0.23\mu\text{m}/\text{pm}$ in the measurement of this lens model. Since, the radial-symmetric defocus term (Z_4) induces a contribution to spherical aberration, the amount of spherical aberration is also expected to vary with wavelength. In Figure 2, we calculate the focus-induced change in spherical aberration and plot it alongside the measured Z_{11} . Also in this figure, the admittedly small, change in the measured 3rd order coma Z_7 is presented as a function of wavelength offset. Defocus and wavelength-induced effects of these and other low-order Zernike modes, such as lateral chromatic aberration are expected and are currently under further experimental investigation.

2.2 Image formation and contrast

Using Finle's PROLITH full-scalar model, we have simulated the image formation of a 2D five-line pattern, where the central line is extended for consideration of the proximity effect. The target linewidth is 150nm for the imaged pattern, with a 300nm pitch (600nm line at the reticle). The objective numerical aperture (NA) is 0.68, conventional illumination has a partial coherence of 0.75 (σ), and exposure wavelength is 248.4nm, assuming a monochromatic source. The following graphs, in Figure 3, show the aerial image intensity of the line-space pattern with 0 μ m, 0.2 μ m, 0.3 μ m and 0.4 μ m of defocus.

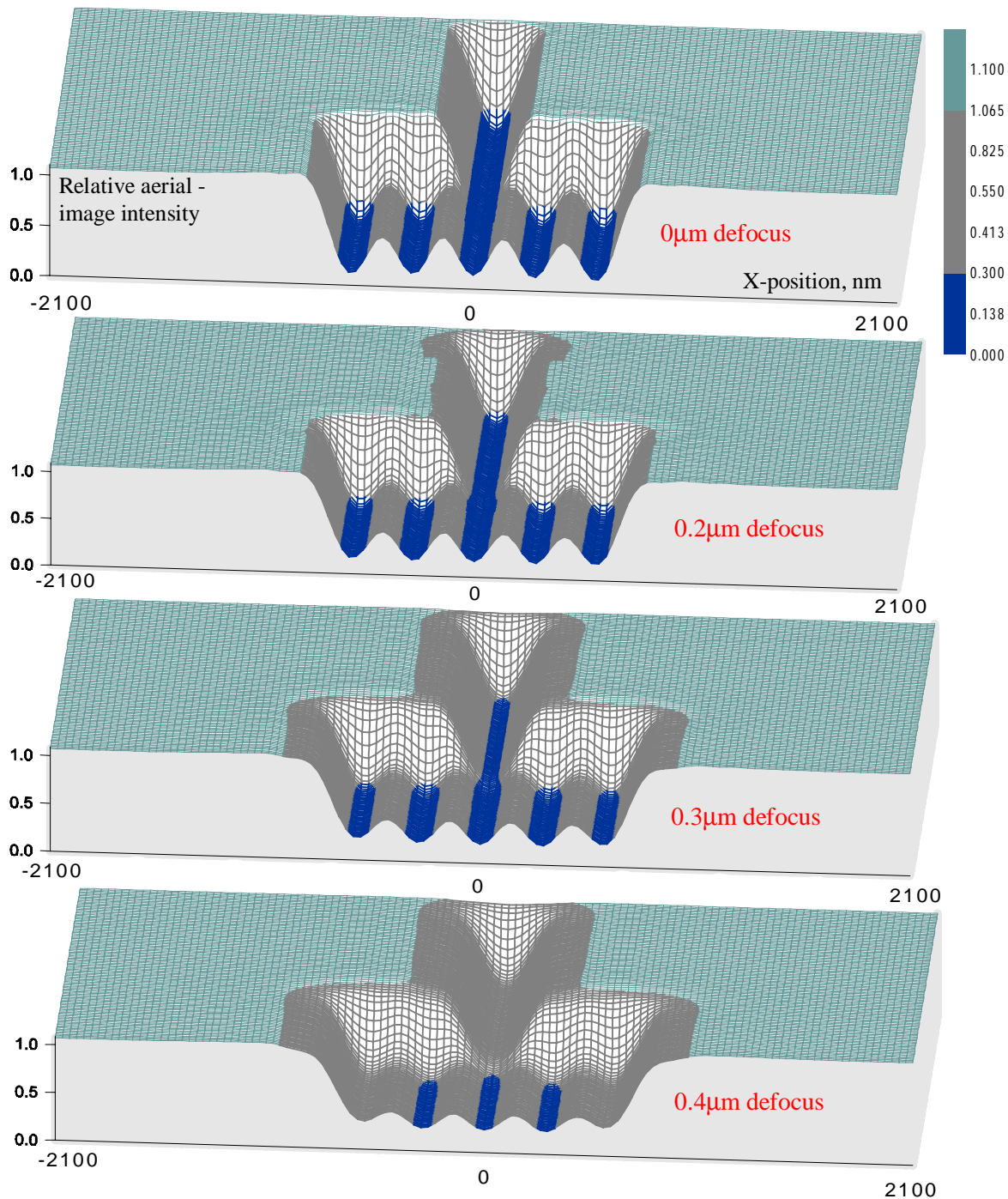


Figure 3. Simulation of 150nm-line aerial image distributions as a function of focus

We can apply a threshold at a fixed relative intensity to estimate the width of the image features and observe the changes with defocus. This raw threshold method is commonly used to significantly simplify the modeling of the photo-activation, diffusion and developer dissolution response of the photoresist. In the figure above, aerial image intensity below the 0.3 threshold is colored with a darker hue. We see that the isolated, dense, and left and right-edge threshold feature widths respond differently to defocus, since the aerial image changes to a different degree depending on the position within the pattern. The slope (or gradient) of the aerial image changes in the region of the fixed threshold, as does the image contrast. Aerial image contrast is typically defined as the ratio of the difference between the maximum and minimum image intensity and their sum, namely:

$$Contrast \equiv \frac{I_{MAX} - I_{MIN}}{I_{MAX} + I_{MIN}}.$$

From the figure above, defocus has a strong impact on the loss of image contrast and therefore image width and shape. Wavelength offset is expected to produce a similar result. Feature geometry, vibrations, illumination-imaging conditions, flare and aberrations also strongly influence the contrast of the aerial image. As shown in the following example, if the aberrations are inferred indirectly from measuring the response of a conventionally-imaged photoresist feature, changes of the image contrast resulting from any of the cited sources, will result in aberration measurement inaccuracy. In addition, changes in the photoresist activation (threshold energy), diffusion and dissolution processes will have an effect on the aerial image ‘sampling’ and may cause additional changes in the measured aberration effect.

The following aerial image simulation is carried out for a five-line array of 150nm dense lines, using the same illumination configuration as above. In this case, we vary the amount of the primary coma aberration ($Z7$) and focus to introduce contrast loss. In figure 4, the resulting aerial images for different levels of the 3rd-order coma aberration are presented at best focus.

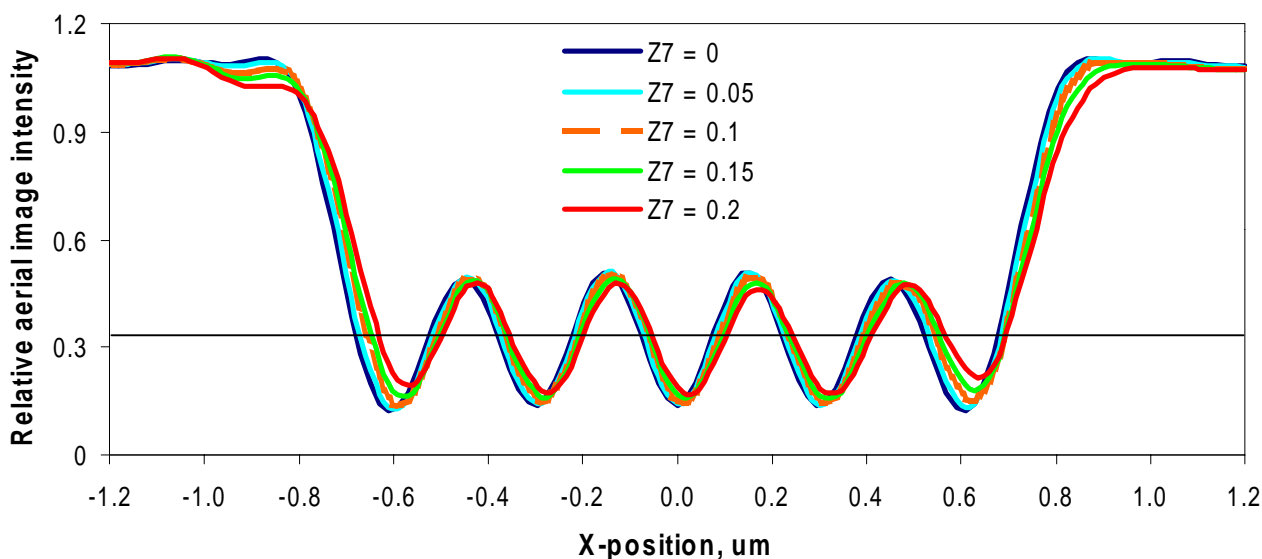


Figure 4. Aerial image of 150nm L/S pattern for different levels of 3rd-order coma aberration

Introduction of the primary coma aberration also results in changes of the aerial image contrast of each feature; again, to different degree depending on the feature position within the array. Due to the $I-\theta$ angular distribution of the coma aberration ($\sim \cos\theta$ or $\sim \sin\theta$, where θ describes pupil azimuth), addition of this type of wavefront error introduces asymmetry to the five-line aerial image. The asymmetry results in a placement offset of the aerial image features relative to the unaberrated image. It also results in image width (shape) differences between the different structures in the five-line array. In practice, it is common to infer the level of the coma aberration by measuring the photoresist linewidth difference between the edge lines in a dense-line array. Typically this metric is referred to as linewidth abnormality (LWA) and is given by the ratio of the difference and sum of the edge-line widths, or in our case:

$$LWA \equiv \frac{L_1 - L_5}{L_1 + L_5},$$

where L_1 is the left and L_5 is the right-edge feature width, as shown in the five-line array cross-section in figure 4. In figure 5, we show a calculation of the linewidth abnormality using a 33% intensity threshold, for the aerial images above and for a set of aerial images with $0.3\mu\text{m}$ defocus (aerial images not shown).

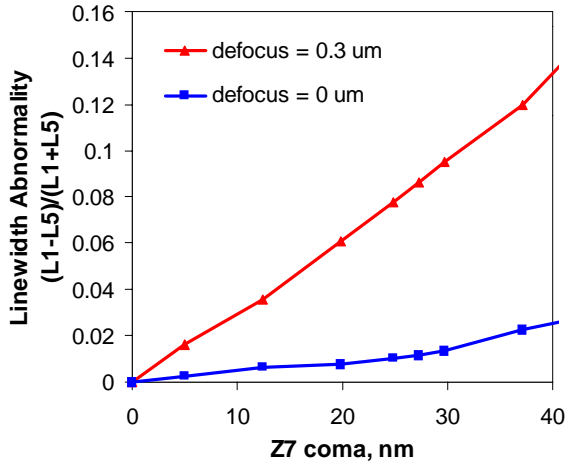


Figure 5. Linewidth abnormality as a function of coma aberration for $0\mu\text{m}$ and $0.3\mu\text{m}$ defocus

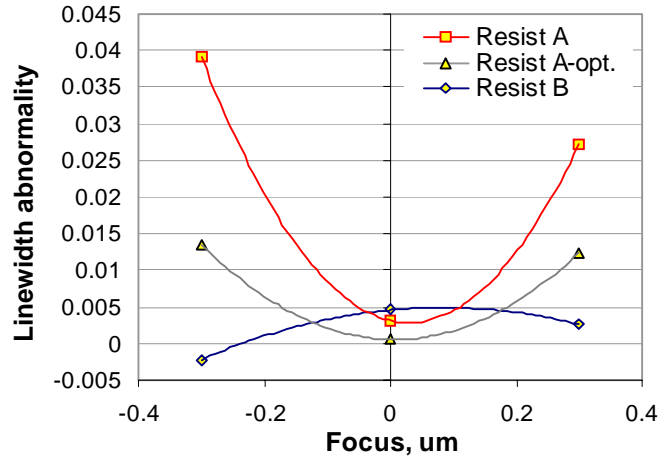


Figure 6. Linewidth abnormality as a function of photoresist process and optimization

From this calculation, we note that the quantity of linewidth abnormality is strongly dependent on defocus and therefore image contrast. As expected, different amounts of coma-induced LWA will be observed as a function of imaging coherence, vibrations, substrate reflectivity, flare, dose, as well as photoresist process response. In this example, we use a 0.33 intensity threshold, however, a photoresist with different photosensitivity will also result in a different level of LWA given an identical aerial image input. In figure 6, experimental linewidth abnormality is presented as a function of photoresist process changes on the EX14C stepper. Due to the number of parameters that affect image contrast or the photoresist process of the test feature, full parametrization of the experimental space is not feasible. This implies an inherent difficulty in quantifying the relationship between lens aberrations and normally imaged photoresist features related to the difficulty in de-coupling aberration-induced contrast changes from other tool/process factors which routinely impact the image contrast in practice.

2.3 Bandwidth effects on image contrast and aberration measurement

The aerial image due to polychromatic illumination is generally computed as an incoherent superposition of aerial images as a function of wavelength, weighted by the spectral intensity,[16,17] or in one dimension,

$$\text{polychromatic aerial image : } I(x) = \int_a^b I(x, Z(\lambda)) \cdot S(\lambda) \cdot d\lambda .$$

Here $I(x, Z(\lambda))$ is the monochromatic aerial image at wavelength λ , with a corresponding level of wavefront error described by $Z(\lambda)$. The weighting function $S(\lambda)$ is the normalized spectral intensity of the illumination source, where $S(\lambda=0)$ is equal to unity. The integration limits a and b define the spectral interval over which the calculation is performed. The summation of the aerial images results in a smearing (blurring) of the composite image in the presence of aberration changes. As we have shown in the previous sections, change in wavelength results in a relatively strong change in the Z focus term ($0.23\mu\text{m}/\text{pm}$) for the given 0.6NA scanner. Therefore, compared to the monochromatic source assumption, aerial image contrast loss is expected for polychromatic illumination; as presented elsewhere.[17,18] The amount of contrast change, however, is dependent on the illumination conditions

and feature (object) properties. Due to this contrast modulation, varied levels of aberration-induced linewidth changes are also expected as a function of illumination bandwidth.

The in-situ interferometer aberration measurement does not suffer to the same degree from the image contrast sensitivity compared to conventionally imaged features. Changes in the contrast of the interferometer diagnostic patterns do result in changes of the sizing of the encoded structures (streets and alleys). However, sizing changes have no effect when a frame-in-frame overlay measurement is employed for measurement of the diagnostic image displacements. Furthermore, since the image is formed through a limiting aperture (effective entrance pupil is $1/10^{\text{th}}$ to $1/15^{\text{th}}$ of the objective numerical aperture), the aerial image of the sub-resolution encoded features is affected more by the transmission of the aperture (aperture size) than focal position or illumination coherence. Due to the reduced effective pupil, the image also has relatively large depth of focus and should be insensitive to typical substrate or image field curvature. The illumination aperture, even at the smallest practical setting, overfills the effective entrance pupil ($\sigma \gg I$), therefore the imaging is incoherent and largely independent of the illumination aperture. The proportionality between the measured image displacement and the phasefront gradient, which is used to reconstruct the measured wavefront is independent of such considerations.

For simplicity, we consider two general types of aberration response to wavelength offset, based on functional parity. We consider a class of odd functions $f(\lambda)$, which can be expressed by $f(\lambda) = -f(-\lambda)$, illustrated schematically by two arbitrary odd functions in the figure 7 example, and even functions, $f(\lambda) = f(-\lambda)$, in figure 8. Over the extent of illumination spectrum, any given aberration response can be approximated by either odd/even form.

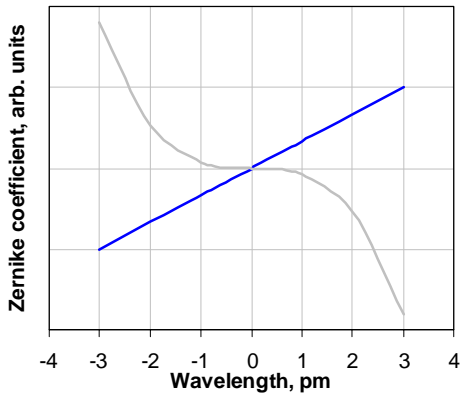


Figure 7. Odd aberration response, $Z(\lambda) = -Z(-\lambda)$

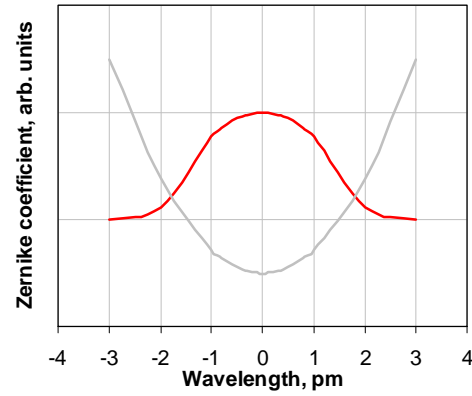


Figure 8. Even aberration response, $Z(\lambda) = Z(-\lambda)$

Therefore, we can generalize the change of any given Zernike coefficient as a function of wavelength by a function of even or odd parity.

In the case of the in-situ interferometer aberration measurement, the effect of an odd-parity aberration-wavelength response would result in a displacement of the diagnostic feature in the $+x$ direction for the $+\lambda$ spectral contribution, and the $-x$ direction for $-\lambda$ (or vice versa, depending on whether the odd aberration-wavelength function is increasing or decreasing with λ). In the case of even-parity aberration-wavelength response, the diagnostic feature shift would be $+x$ for $+\lambda$ spectral contribution and $+x$ for $-\lambda$ (or $-x$ in both cases). Therefore the imaged diagnostic feature would exhibit a shift towards $+x$ (or $-x$). In both cases, the resulting measured aberration can be expressed as the weighted average of the aberration-wavelength response $Z(\lambda)$ on an interval $\langle a, b \rangle$, namely:

$$\text{measured } Z_N = \frac{1}{b-a} \int_a^b Z(\lambda) \cdot S(\lambda) \cdot d\lambda .$$

The weighting function $S(\lambda)$ expresses the normalized spectral intensity, where $S(\lambda=0)$ is equal to unity and $Z(\lambda)$ is the aberration-wavelength response. Therefore, for symmetric illumination spectra, the odd aberration-wavelength response will be largely insensitive to changes of the spectral width, since the weighted average of $Z(\lambda)$ will approach $Z(\lambda=0)$. The in-situ interferometer results of an even-parity aberration-wavelength response will be a function of source spectral width.

3. BANDWIDTH: IN-SITU INTERFEROMETER EXPERIMENTAL RESULTS

Using the Litel interferometer technique, lens aberrations have been characterized for a Nikon EX-14C step-and-repeat and S-202A scan-and-repeat exposure system, with maximum lens numerical aperture of 0.6 and partial coherence of 0.75. All experiments in this study were carried out in static exposure mode on photoresist-coated, bare-silicon substrates (with only a native oxide). The photoresist imaging was done in the Shipley UV5 resist with AR2 inorganic bottom anti-reflective coating (*BARC*) for the EX-14C. In the case of the S-202 scanner, a Shipley APEX-E/CD-11 (Brewer Science *BARC*) process was used. Overlay metrology (frame-in-frame image-placement measurement of the interferometer diagnostic features relative to a reference grid) was done using KLA-5520 and KLA-5200XP tools.

Cymer ELS-5400 laser sources were used with both exposure systems in this report. Modification of the laser bandwidth output was achieved by mechanical adjustment of the line-narrowing optics dispersion, gas composition, or other techniques. The full-width-at-half-maximum (*FWHM*) of the spectrum was measured using an on-board metrology capability of Cymer excimer lasers. The width of the spectrum at the 95% level of the energy integral (*E95%*) was acquired by varied spectroscopic techniques. The wavelength offsets, for characterization of the lens aberration-wavelength response in the previous sections, was achieved by software control of the laser line-narrowing module. The wavelength was calibrated to a laser-internal atomic wavelength reference.

In Figures 9 and 10, below, the response of the primary coma and spherical aberration terms to *FWHM* bandwidth changes is presented, for two field points measured on the EX-14C. Three *FWHM* bandwidth conditions were achieved in this set of experiments, namely, 0.41pm (nominal operation), 0.5pm and 1pm. The *E95%* bandwidth was not captured in this case.

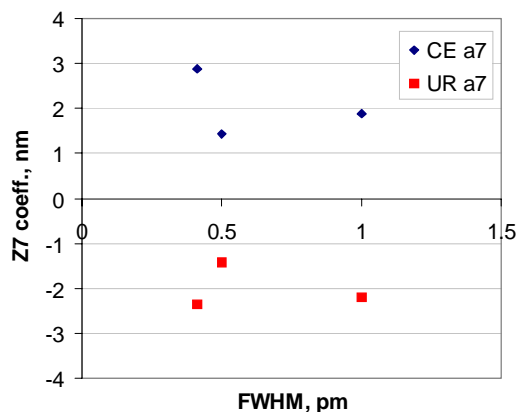


Figure 9. Primary coma response to FWHM

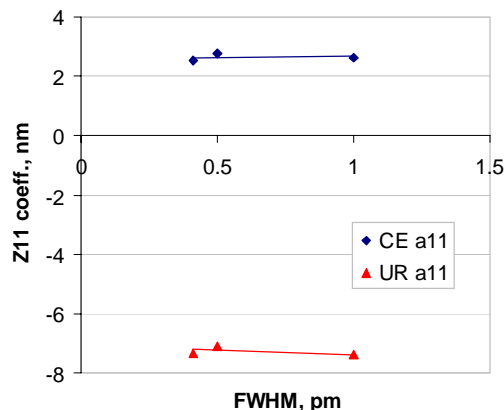


Figure 10. 3rd-order spherical response to FWHM

Here, *CE* represents a point in the field center (x, y coordinates at the image plane: $\langle x, y \rangle = \langle +I, +I \rangle$ mm, relative to and origin $\langle 0, 0 \rangle$ at the image field center) and *UR* is the upper-right field corner (x, y coordinates at the image plane $\langle x, y \rangle = \langle +9, +9 \rangle$ mm) for a 22x22mm maximum square stepper field. As expected, we note a difference in the magnitude of the Zernike coefficients between the field center and edge, the field center exhibiting lower aberration response. For both field points, the primary coma aberration slightly increases with *FWHM* bandwidth. On the other hand, the changes in the spherical aberration between conditions are less than 0.2nm, which is on the order of the currently cited reproducibility of this measurement.[14] This observed difference in aberration-wavelength response for the two terms may be due to differences in the functional parity, as discussed in the previous section.

The root sum square (referred to as *RMS*) of 24 Zernike coefficients (*Z5* to *Z28* included; piston, x/y tilt and focus terms excluded) has been calculated for this system, as a function of *FWHM*. This result is presented in Figure 11 for three points in the square stepper field, two in the field center (labeled *CE-1* and *CE-2*) and one in upper-right corner $\langle +9, +9 \rangle$ mm. The data in this graph is normalized relative to the *RMS* result at 0.41pm *FWHM* at the *CE-2*

field point, so that RMS at 0.41pm FWHM is equal to unity and all other RMS results are scaled relative to this RMS value.

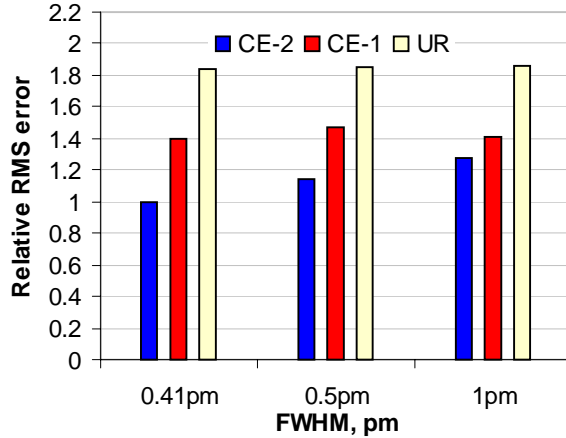


Figure 11. Relative RMS wavefront error, EX-14C

The result in figure 11 shows the behavior of the RMS wavefront response ($Z5$ to $Z28$) to the change in bandwidth for three points in the stepper field. The most dramatic change in RMS wavefront is observed for *CE-2*, exhibiting a 20% increase, which is approximately three times less than the cross-field RMS variation. The other two field points, however, show relative insensitivity to laser FWHM bandwidth changes. The cause of this difference in behavior of the two adjacent CE points (separated by ~2mm at the image field) is not determined at this time.

The following graph, figure 12, summarizes the RMS results for the S-202 scanner for a series of bandwidth settings, as follows, 0.35pm (1.4pm E95%), 0.4pm (1.4pm E95%), 0.6pm (1.6pm, 1.9pm, 2.7pm E95%), and 2.0pm (3.5pm, 6pm E95%). Here we consider five points within the static scanner field (covering both the parallel and orthogonal directions relative to the scan direction), labeled FP1 through FP5; the data is ordered by ascending bandwidth conditions and is not normalized.

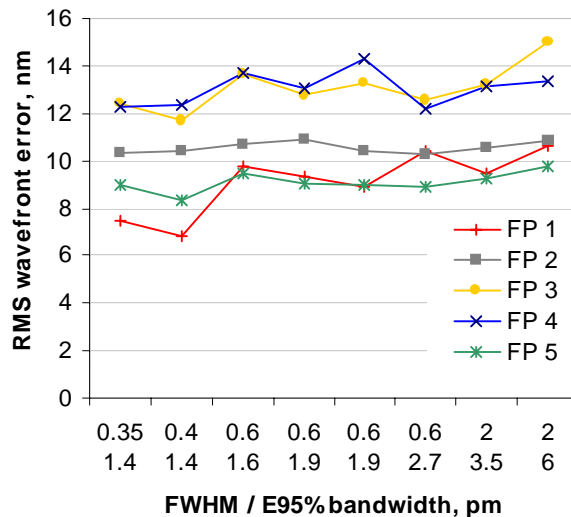


Figure 12. RMS wavefront error results summary, S-202

As seen in the stepper data, large RMS error differences exist across the image field, almost 4nm of cross-field RMS variation is observed in the case of this scanner, under static exposure conditions. The cross-field variation in the aberrations is reduced (via aberration averaging along the scan direction) under typical scanning exposure. The

overall aberration of this system is very good given the imaging impacts presented in section 2.2 or elsewhere.[3-5] The results in figure 12 show a positive trend with the increase in bandwidth, and appear relatively consistent for the five points tested. Noticeably, FP-1, FP-3 and FP-5 exhibit stronger dependence on bandwidth than FP-2 and FP-4. We can plot the RMS error as a function of FWHM or E95% bandwidth and can fit this response using a linear regression approximation. This result is shown in figure 13 (for FWHM) and figure 14 (for E95%), as follows; only the first three field points are plotted for visual clarity.

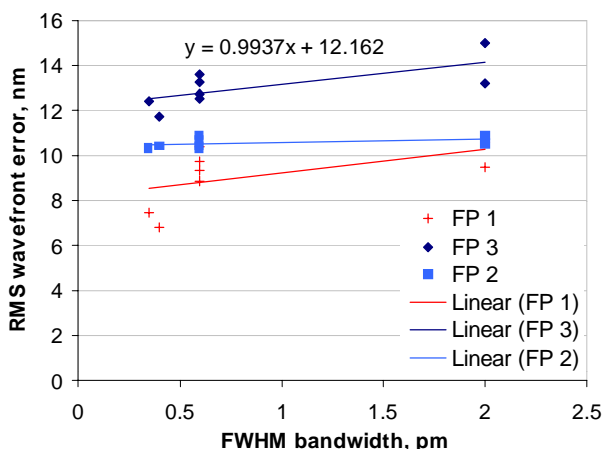


Figure 13. RMS wavefront error vs. FWHM bandwidth

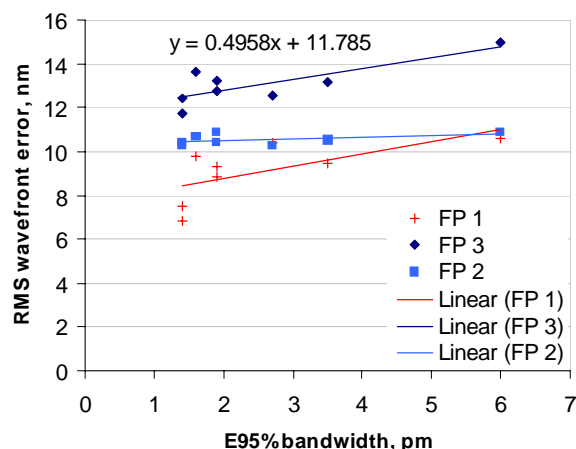


Figure 14. RMS error vs. E95% bandwidth

The equation of the linear RMS-bandwidth relationship for field point 3 is displayed in figures 13 and 14. We also calculate the average of the slopes for the five different field points. The average RMS/bandwidth slopes are 0.57nm/pm +/- and 0.28nm/pm for FWHM and E95% respectively. Increased sampling (wafer exposures) at the same bandwidth condition is necessary to consider the statistical significance of these results. At present, the resulting slopes are largely dominated by the extreme (maximum and minimum) BW conditions.

4. SUMMARY AND CONCLUSIONS

In this work we have considered the impact of contrast-loss on aerial image formation and measurement of projection objective aberrations. Lithography simulations were employed in order to demonstrate the difficulties in inference of lens aberrations from conventional photoresist image analysis, related to de-coupling of the aberration-induced from other tool/process sources of interaction with the aerial image. The image-feature response of a five-line pattern was examined as a function of focus (Z_4) and primary coma aberration (Z_7). Experimental in-situ interferometer measurements of the aberration-wavelength response for focus $Z_4(\lambda)$, 3rd-order spherical $Z_{11}(\lambda)$ and primary coma $Z_7(\lambda)$ were also shown. When considering polychromatic illumination, inclusion of the aberration-wavelength response is necessary as it impacts aerial image formation. The expected response of the in-situ interferometer aberration-measurement technique as a function of spectral width is discussed for $Z(\lambda)$ functions of even and odd parity. Finally, aberration measurement results as a function of laser spectral bandwidth were discussed for a 0.6NA KrF stepper and scanner system.

We show an increase in the measured aberration RMS as a function of bandwidth in the case of the scanner, which can be linearly approximated. In both the stepper and scanner case, differences in the aberration-bandwidth response are observed as a function of field location. The magnitude of the cross-field RMS variation is more than two times of that induced by bandwidth changes over the experimental conditions. Further experimental investigation is required to correlate the functional parity of the aberration-wavelength response and measured aberration changes as a function of bandwidth. At present, results of full characterizations of the aberration-wavelength response $Z(\lambda)$ are used in simulation models to predict the impact on photoresist imaging.

ACKNOWLEDGMENTS

The author would like to acknowledge the personnel at Hewlett-Packard TDC, Fort Collins, CO and HP ULSI Labs, Palo Alto, CA (now Agilent Technologies) for management, experimental support and discussions.

REFERENCES

- [1] Experiments carried out at Hewlett-Packard/Agilent Technologies ULSI Labs, Palo Alto, CA and ICBF B2-Fab, Fort Collins, CO.
- [2] "Behavior of lens aberrations as a function of wavelength on KrF and ArF lithography scanners," Mark Terry, Ivan Lalovic, Greg Wells, Adlai Smith, to be presented at SPIE Microlithography XIV, Proc. Vol. **4346** (2001).
- [3] T.A. Brunner, "Impact of lens aberrations on optical lithography," Proc. Interface '96, San Diego, CA, 1 (1996).
- [4] D.G. Flagello, et. al., "Towards a comprehensive control of full-field image quality in optical photolithography," Proc. SPIE **3051**, 672 (1997).
- [5] J. Grotych and D. Williamson, "Effects of higher order aberration on the process window," Proc. SPIE **1463**, 368, (1991).
- [6] D. Malacara, ed., *Optical Shop Testing*, Wiley, New York (1977).
- [7] V.N. Mahajan, *Optical Imaging and Aberrations, Part I*, SPIE OE Press, Bellingham, WA, 173-178 (1998).
- [8] J.P. Kirk, "Astigmatism and field curvature from pin-bars," Proc. SPIE **1463**, 282 (1991).
- [9] J.P. Kirk, C.J. Proglor, "Application of blazed gratings for determination of equivalent azimuthal aberrations," Proc. SPIE **3679**, 70 (1999).
- [10] A.R. Neureuther, et. al., "Modeling defect-feature interactions in the presence of aberrations," Proc. BACUS **4186-42** (2000).
- [11] P. Dirksen, et. al., "Novel aberration monitor for optical lithography," Proc. SPIE **3679**, 79 (1999).
- [12] A.H. Smith, B. McArthur, R. Hunter, "Apparatus, Method of Measurement and Method of Data Analysis for Correction of Optical System," US patent 5,828,455, Oct. 27, 1998.
- [13] K. Rebitz, A.L. Smith, "Characterizing exposure tool optics in the fab," *Microlithography World*, 10-14, summer (1999).
- [14] N.R. Farrar, et. al., "In-situ measurement of lens aberrations," Proc. SPIE **4000**, 18 (2000).
- [15] V. Mahajan, "Zernike Annular Polynomials for Imaging Systems with Annular Pupils," *Opt. Soc. Am.*, 342-352 (1981).
- [16] P. Yan, et. al., "Effects of chromatic aberration in excimer laser lithography," Proc. SPIE **1674**, 316 (1992).
- [17] A. Kroyan, et. al., "Modeling the effects of eximer laser bandwidths on lithographic performance," Proc. SPIE **4000**, 658 (2000).
- [18] "Effects of E95% integral vs. FWHM bandwidth specifications on lithographic imaging," A. Kroyan, I. Lalovic, N. Farrar, to be presented at SPIE Microlithography XIV, Proc. Vol. 4346 (2001).